REVIEW

Check for updates

Two-dimensional metal organic framework nanosheets in electrocatalysis

Ping Wang, Cheng Yang, Jiasai Yao, Huawei Li, Zikang Hu and Zhenxing Li [iD] *

The thin layered structure and porous structure in two-dimensional metal organic framework (2D MOF) nanosheets have rapidly emerged as promising catalytic materials in the electrocatalytic reaction, because 2D MOF nanosheets not only provide larger active surface area, more edge active sites, and larger activation surface area, but they can also achieve rapid mass transfer and accelerate the reaction process in catalytic reactions. However, despite extensive research, the practical application of 2D MOFs remains limited due to challenges in scalability, stability, and integration with real-world devices. Herein, we summarized the latest progress in the deliberate engineering of 2D MOF nanosheets as a catalyst for electrocatalytic reactions, with a particular focus on their electrocatalytic and energy-related applications. The two major synthetic pathways of 2D MOF nanosheets are reviewed, including the top-down method and bottom-up method, and the recent development of synthetic methods is also discussed. Unlike existing reviews that primarily focus on theoretical aspects or specific applications, this work integrates insights from both experimental and computational studies, offering a holistic view of the field. This review highlights the importance of rational material design, scalable synthesis methods, and robust performance evaluation protocols. By bridging the gap between fundamental research and practical application, this review aims to accelerate the transition of 2D MOFs from laboratory-scale studies to real-world solutions, ultimately contributing to the development of sustainable and efficient energy systems.

Introduction

Due to the flexible and adjustable functional groups, large specific surface and porous structure, MOFs have emerged as a key research area in the area of material chemistry during the past several years, and have rapidly achieved a series of outstanding research results.[1-4] Thanks to these properties, MOFs hold significant potential across a wide range of applications, encompassing areas such as catalysis, biomedicine, sensors, material separation and storage, and energy storage and conversion.[5-12] Since 2D MOF nanosheets combine the features of MOFs and 2D nanomaterials, 2D MOF nanosheets expose more active sites on their surface than bulk MOF materials, and can obtain ultra-large porosity by extending the interlayer distance. These properties of 2D MOFs result in the

College of New Energy and Materials, China University of Petroleum (Beijing), Beijing 102249, China. E-mail: lizx@cup.edu.cn

Ping Wang received her Master's degree from the China University of Petroleum (Beijing) in 2022. She is a PhD student under the supervision of Prof. Zhenxing Li at the College of New Energy and Materials, China University of Petroleum (Beijing), China. Her current research interests are the synthesis and application of functional nanomaterials.

Ping Wang

Cheng Yang was born in 2000 in Sichuan province, China. He obtained his Master's degree from the College of New Energy and Materials, China University of Petroleum (2024). He is currently pursuing his PhD degree at the College of New Energy and Materials, China University of Petroleum (Beijing). His research interest is the applications of alloys in electrocatalysis.

Cheng Yang

improvement of the reactivity and catalytic activity in separation, sensing, catalysis, etc.[13–16] There are two main methods for preparing 2D MOF nanosheets: bottom-up and top-down. The bottom-up synthesis approach mainly realizes the construction of organic ligands and metal ion precursors directly through the coordination interactions at interfaces such as gas/liquid or liquid/liquid, which are gentler and more controllable, and effectively limit the vertical growth of MOFs.[17–19] However, the production yield of MOF nanosheets employing the bottom-up approach is largely determined by the interfacial area, which limits the massive production of MOF nanosheets. Because of the large surface energy, the formed 2D MOF nanosheets tend to reaggregate into bulk structures. The top-down fabrication strategy uses mechanical forces (sonication or grinding) to overcome fragile interlayer interactions, including hydrogen bonding or van der Waals forces to peel off and disperse 2D MOF nanosheets. By selecting solvents that have suitable surface tension properties, such as acetone, tetrahydrofuran, and N,N-dimethylformamide (DMF), researchers were able to efficiently exfoliate lamellar bulk MOFs during ultrasound sonication.[20–24] While the ultrasonic exfoliation method is simple and effective, it also faces the problem of restacking. Therefore, the production of 2D MOF nanosheets with effective dispersion remains a challenging task.

In the catalytic reaction, 2D MOF nanosheets offer a greater active surface area and a higher number of edge active sites in comparison with bulk MOFs. The composition and structure of 2D MOF nanosheets can be tailored by adjusting the metal nodes and organic linkers. This tunability allows for the optimization of catalytic properties, such as selectivity and activity, for specific electrocatalytic reactions. And 2D MOF nanosheets can achieve rapid mass transfer and accelerate the reaction process in catalytic reactions. As for electrical performance, the traditional bulk MOF exhibits extremely low volumetric conductivity (10^{-12} to 10^{-8} S cm^{-1})[25,26] and weak magnetic coupling due to large separated metal centers, such as polyatomic and insulating organic ligands. However, the conjugated 2D MOF nanosheets synthesized using planar organic ligands as structural directing agents and square metal complexes not only exhibit high conductivity ($>10^{-3}$ S cm^{-1}),[26] but the highly delocalized π electrons on the 2D plane also drive magnetic ordering through interactions between charge carriers and local spins,[27,28] making conjugated 2D MOF nanosheets an interesting candidate for ferromagnetic semiconductors.[6,28–30] Therefore, in electrocatalytic reactions, the 2D MOF nanosheet morphology exhibits excellent performance and enormous potential.[11] However, many 2D MOF nanosheets suffer from poor stability in electrochemical environments, leading to degradation and loss of catalytic activity.

Jiasai Yao received his Master's degree from the China University of Petroleum (Beijing) in 2022. He is currently pursuing his PhD degree at the College of New Energy and Materials, China University of Petroleum (Beijing). His current research interest is the synthesis and application of functional nanomaterials.

Jiasai Yao

ZiKang Hu was born in 1998 in Hubei province. She obtained her Master's degree from the College of Pharmacy, South-Central Minzu University (2023). She is currently pursuing her PhD degree at the College of New Energy and Materials, China University of Petroleum (Beijing). Her research interest is the application of rare earth MOFs in photocatalysis.

Zikang Hu

Huawei Li was born in 1997 in Anhui province. He obtained his Master's degree from the College of New Energy and Materials, China University of Petroleum (2023). He is currently pursuing his PhD degree at the College of New Energy and Materials, China University of Petroleum (Beijing). His research interest is the application of rare earth alloys in electrocatalysis.

Huawei Li

Zhenxing Li obtained his PhD (2011) from the Peking University of China. He is now a Professor at the State Key Laboratory of Heavy Oil Processing and College of New Energy and Materials at the China University of Petroleum (Beijing). His recent research interests focus on the design and synthesis of porous materials and rare earth-based nanomaterials for application in electrocatalysis and photocatalysis.
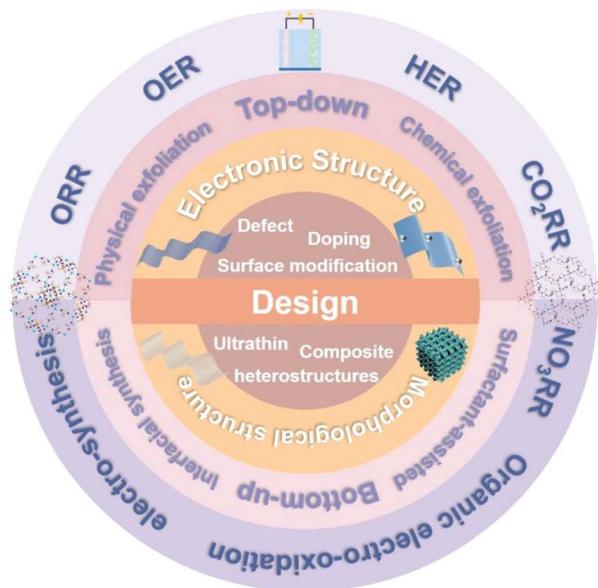
Zhenxing Li

Fig. 1 Design and application of MOF nanosheets.

And effective integration of 2D MOF nanosheets with electrode materials remains a challenge. Poor contact between the nanosheets and the electrode substrate can hinder electron transfer and reduce overall performance.

The electrocatalytic reactions have significant applications in the realms of environmental protection, chemical synthesis and energy conversion. Particularly in the domain of energy conversion, many renewable energy systems have emerged, such as water electrolysis reactions,[31] the oxygen reduction reaction (ORR),[32] the nitrogen reduction reaction (NRR)[33] and the carbon dioxide reduction reaction (CO₂RR).[34,35] Utilizing electrical energy to overcome thermodynamic barriers and optimize some high-energy-consuming chemical reactions into efficient and green economic production routes is highly promising. For example, reactions developed in recent years include the electrooxidation of organics (methanol oxidation and glycerol oxidation),[36,37] hydrogenation of acetylene, and synthesis of C–N coupling products.[38] However, the development of electrocatalysts remains the key to further advancing the application of electrocatalytic reactions.

Overall, the flexible and adjustable metal active sites in MOF materials have great potential for application in electrocatalytic reactions. Moreover, as part of the 2D nanosheet material category, 2D MOF nanosheets integrate the advantages of both porous materials and 2D materials, and have great development prospects. However, the design of ultra-thin nanosheets and the active site structures remain key and challenging for enhancing the catalytic performance of 2D MOF nanosheets. Therefore, this article reviews the recently developed 2D MOF nanosheet materials with excellent catalytic performance for electrocatalytic reactions. Then, the main preparation methods of 2D MOF nanosheets are highlighted, as well as the design strategies for high-efficiency electrocatalytic activity, to guide catalyst structure design, and the existing problems and prospects were

elucidated. This review can help readers quickly understand 2D MOF nanosheets and their prospective employment (Fig. 1).

Synthesis of 2D MOF nanosheets

The perfect construction of nanosheet structures is the key to catalytic activity. The preparation approaches of MOF nanosheets mainly include two directions: bottom-up and top-down. The advantages and disadvantages of different synthetic pathways are shown in Table 1. A more common characterization would be exfoliation and growth (Scheme 1).

Top-down method

The top-down method is a synthesis technique that generates nanostructures by deconstructing larger materials.[21] This method is mainly applicable to layered MOF materials that are quite weak. Researchers disrupt the weak interlayer interactions in bulk MOFs by applying external driving forces, thereby producing 2D MOF nanosheets. According to different external conditions applied, it is primarily categorized into two types: chemical peeling and physical peeling. The physical exfoliation approach is better suited for layered MOF materials, whose weak interlayer interactions can be destroyed by simple ultrasonic or grinding methods. The chemical exfoliation method can break strong interlayer interactions, and this method also enables more straightforward control over the nanosheets' morphology and structure.

Sonication exfoliation

Ultrasound exfoliation is a simple and efficient method that utilizes the energy released from the explosion of microbubbles generated by ultrasound to rapidly create a local high-temperature and high-pressure environment, which disrupts the interlayer interactions in bulk MOFs, achieving the exfoliation of 2D nanosheets. Zamora and colleagues[39] utilized an ultrasonic treatment to disrupt the fragile π–π stacking interactions in bulk $[Cu_2Br(IN)_2]_n$, thereby producing extremely thin $[Cu_2Br(IN)_2]_n$ nanosheets with a thickness of approximately 5 nm in an aqueous solution (Fig. 2a and b). Motivated by this pioneering research, the technique of sonication exfoliation was subsequently gained adopted for the production of MOF nanosheets.[1,44,45] At the same time, researchers have conducted extensive studies on the two main factors of liquid phase solvent selection and the duration of ultrasonic treatment, as these factors significantly influence the nanosheets' crystalline structure and thickness. Chandrasekhar et al.[46] investigated the effect of exfoliating Cd-TPA MOFs by breaking their interlayer hydrogen bonds in various solvents such as ethanol and ethane on the fluorescence properties of the MOF nanosheet materials. Dimethyl sulfoxide (DMSO) showed the highest quantum yield. Ma et al.[41] studied the exfoliation performance of various solvents including ethanol, methanol, isopropanol, DMF, and n-hexanol for liquid-phase exfoliation of ZSB-1 $(Zn_2(SBA)_2(BPTP))$ nanosheets. The results indicated that only n-hexanol could successfully exfoliate the ZSB-1 nanosheets (Fig. 2d–g), as n-hexanol has a stronger binding effect on the ZSB-1 nanosheets.

Table 1 The summary of different synthetic pathways

Method/technique	Advantages	Disadvantages
Sonication exfoliation	1. Promotes MOF formation through cavitation	1. Requires combination with other methods (*e.g.*, ball milling) for optimal results
	2. Reduces particle aggregation effectively	2. Potential structural damage from an intense energy input
	3. Facilitates solvent infiltration between layers	3. Needs post-treatment stabilization (*e.g.*, propanol solvent)
	4. Enables efficient nanosheet exfoliation	4. Limited effectiveness on certain bulk precursors
	5. Works synergistically with mechanical methods	5. Requires precise parameter control (time and frequency)
Micromechanical exfoliation	1. Produces 2D MOFs with pristine surfaces	1. Limited to few types of MOF nanosheets
	2. Generates large lateral dimensions (∼10 μm)	2. Requires delicate starting crystals
	3. Maintains superior crystallinity	3. Potential low yield due to material fragility
	4. Minimal chemical contamination	4. Energy-intensive process (freeze–thaw cycles)
	5. Scalable shear force generation method	5. Requires precise temperature control
Chemical reduction method	1. Wide control range over the exfoliation process	1. Requires specific chemical intercalants (*e.g.*, trimethylphosphine)
	2. High yield of MOF nanosheets	2. Potential structure damage during cleavage
	3. Ultrathin thickness achievable (1 nm)	3. Time-consuming multi-step process
	4. Precise thickness control through reagent quantity adjustment	4. Specialized equipment needed for chemical treatment
	5. Applicable to various layered MOF structures	5. Possible residue contamination from intercalants
Interfacial synthesis method	1. Ultrathin nanostructures confined by reaction space	1. Limited interfacial area may restrict production yield
	2. Allows natural precipitation of nanosheets from the interface	2. Requires precise control of solvent layers and concentrations
	3. Facilitates size control (0.5–4 μm lateral dimensions achieved)	3. Complex setup with multiple immiscible solvents needed
	4. Offers flexibility in material property adjustment	4. Time-consuming diffusion-controlled process
	5. Enhances crystallinity through controlled ion diffusion	5. Potential scalability challenges for industrial applications
Surfactant-assisted method	1. Enables directional control of crystal growth	1. Surfactants/capping agents adhere to MOF surfaces, covering active sites
	2. Facilitates 2D structure formation by competitive coordination with metal nodes	2. Residual additives may impair electrochemical performance due to blocked active sites
	3. Compatible with diverse surfactants (CTAB, PVP, and SDS) and small capping molecules (formic acid, *etc.*)	3. Potential requirement for additional purification steps to remove additives
	4. Allow synthesis under mild conditions (*e.g.*, 25 °C)	4. Limited thermal stability of surfactants may restrict high-temperature applications
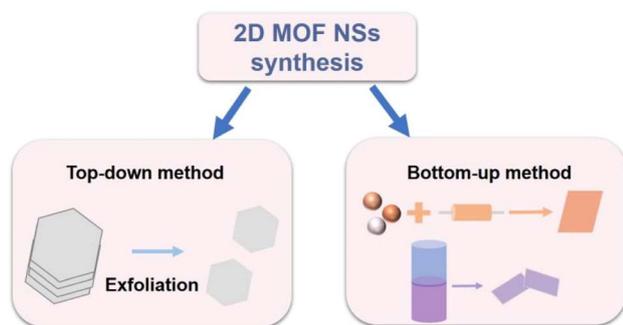
Scheme 1 Synthesis process of 2D MOF nanosheets.

The interactions with solvents can induce irreversible structural transformations, which facilitate the generation of 2D nanosheets during ultrasonic processing. Israr and colleagues explored how binary or ternary solvent mixtures influence the structural properties of MOF nanosheets, and their findings indicated that the yield of MOFs reached a maximum when employing a ternary mixture of ethanol, DMF and water, with an ultrasonic power setting of 750 W and treatment time of 2 hours (Fig. 2c).[40] Several additional studies have highlighted the significance of the appropriate solvent in the ultrasonic delamination of layered MOFs.[47,48] The impact of ultrasonic duration on MOF synthesis and morphological structure has been extensively studied. Li *et al.* successfully prepared $Cu_3(BTC)_2$ nanocrystals using an ultrasonic bath and investigated the MOF yield under different ultrasonic durations, finding that extended reaction durations notably improved MOF output.[49] Additionally, extended ultrasonic treatment times altered the morphology and dimensions of the MOFs, causing a transition from spherical particles to 2D needle-like
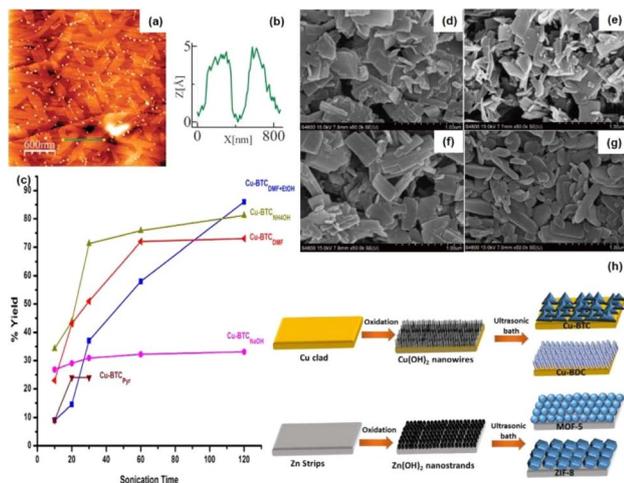
Fig. 2 (a) Atomic force microscopy (AFM) phase image of $[Cu_2Br(IN)_2]_n$ nanosheets obtained by sonication exfoliation. (b) The height of nanosheets in Fig. 1a (green line). Adapted from ref. 39. (c) The relationship between organic solvents, ultrasonic treatment time, and MOF yield.[40] The Scanning Electron Microscopy (SEM) images of ZSB-1 ultrasonically treated in (d) ethanol, (e) n-hexyl alcohol, (f) methanol and (g) DMF.[41] (h) Diagrammatic representation of the procedure for creating MOF thin films on a metal substrate.[42,43]

structures, with the size increasing 9 times. The use of ultrasound can enhance the uniformity and crystallinity of MOF crystals.

By precisely controlling the energy input, unnecessary side reactions and framework destruction can be reduced, resulting in higher quality 2D MOF nanosheets. Therefore, many ultrasound-assisted synthesis methods have been developed. For example, Zhao et al. utilized ultrasound to create a local high temperature and high-pressure environment through the energy released by microbubble implosions in a "hot spot" for the preparation of 2D MOF nanosheets, successfully constructing extremely thin NiCo-BDC nanosheets.[50] This method also has a certain degree of versatility, providing a new synthetic pathway for the formation of MOF nanosheets, such as Mn-BDC, NiFe-BDC, and $Zn(BDC)(H_2O)_n$. Moreover, researchers utilized the mechanical waves and cavitation effects produced by ultrasound to assist in exfoliation, which not only significantly reduced synthesis time but also enabled the production of MOF crystals much smaller than those made by traditional methods. For instance, Vaitsis et al. synthesized an MOF-5 material using ultrasound-assisted methods, resulting in crystals that were 60 times smaller than those prepared by traditional methods, and the duration for synthesis has been shortened from 24 hours to just 30 minutes (Fig. 2h).[42] Ultrasonic waves can also be combined with other methods, such as ball milling, to further optimize the synthesis of MOFs. Zhao et al.[51] successfully prepared nickel-based MOFs by combining ultrasonic waves with ball milling. The ultrasonic waves promoted the formation of Ni-MOFs and reduced aggregation, whereas ball milling inhibited grain growth and refined the crystal particles. Yang and colleagues combined dual solvent ultrasonic treatment with wet ball milling to derive $Zn_2(bim)_4$

nanosheets from bulk precursors.[44] The wet ball milling method enabled the infiltration of methanol molecules between the layers of bulk MOFs, thereby weakening the interlayer interactions, Propanol solvent was subsequently employed to stabilize the exfoliated $Zn_2(bim)_4$ nanosheets.

Micromechanical exfoliation

This technology utilizes mechanical force to overcome the intermolecular interactions between layered materials, thereby achieving exfoliation.[43,52] It typically produces 2D MOF nanosheets characterized by micrometer-scale lateral dimensions and extremely thin thicknesses. The micro-mechanical exfoliation technique is mainly divided into tape technology and freeze-thaw technology. Tape technology was first developed for the exfoliation of graphene and has since been extended to various ultrathin 2D materials. Coronado et al. first triumphantly synthesized a layered structure of $Fe(bimCl)_2$ (HbimCl = 5-chloro-functionalized benzimidazole), and then used plastic tape to exfoliate the bulk MOFs to produce $Fe(bimCl)_2$ nanosheets (Fig. 3a).[53] Similarly, a new micro-mechanical exfoliation approach known as the freeze-thaw technique was introduced by Zhao's group. During this procedure, bulk MOF crystals are initially scattered in hexane, subsequently frozen in liquid nitrogen and finally thawed in a hot water bath (Fig. 3b). The volume changes during the freeze–thaw cycles generate shear forces, allowing the formation of MOF nanosheets.[54] The prepared MOF nanosheets display consistent, substantial lateral dimensions of approximately 10 μm, and a thickness of 4 nm (Fig. 3c and d). Owing to the delicate nature of the initial crystals, the micro-mechanical exfoliation method can only produce a few types of MOF nanosheets, but this method shows
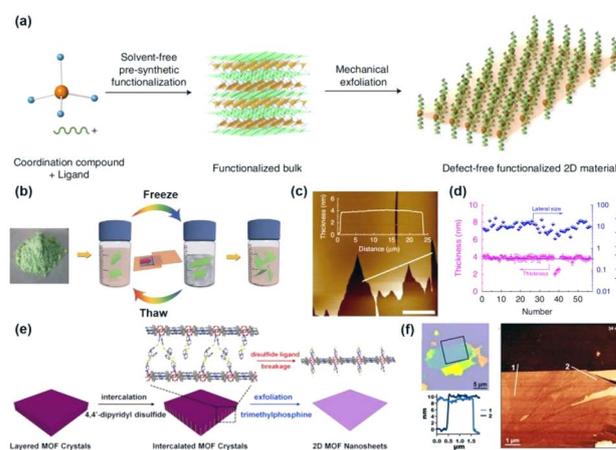

Fig. 3 (a) Diagrammatic representation of the pre-synthesized functionalized MOF. The functionalized bulk MOF was synthesized first. Mechanical exfoliation cannot modify the arrangement of functional groups on the surface.[53] (b) Schematic illustration of the freeze–thaw exfoliation approach. (c) AFM image of MAMS-1 nanosheets (MAMS-1 NSs). (d) The lateral size and thickness distribution of MAMS-1 NSs obtained by freeze–thaw exfoliation (the horizontal line denotes the theoretical thickness of MAMS-1 NSs).[54] (e) Schematic illustration of $Zn_2(PdTCPP)$ exfoliation.[55] (f) Optical image of 2D MOF nanosheets along with their AFM image and layer thickness. Adopted from ref. 56.

significant potential for the production of 2D MOFs that feature pristine surfaces, expansive lateral dimensions, and superior crystallinity.[57]

Chemical reduction method

Chemical exfoliation is a process that separates the layers of layered materials through chemical reactions, which can be employed to fabricate MOF nanosheets with specific functions and structures. These 2D MOF nanosheets possess unique properties due to their adjustable pore sizes and high surface area, making them potentially worthwhile for applications in the area of electrocatalysis. Some research results indicate that solvent intercalation can disrupt the interlayer interactions within MOFs, thereby yielding 2D MOF nanosheets. For example, Zamora's team reported the use of water molecules (H_2O) to infiltrate the interlayer positions of the layered $[Cu(mpym_2S_2)(m-Cl)]_nSnH_2O$ (pym_2S_2 = dipyrimidine disulphide), weakening its interlayer interactions and successfully preparing ultrathin MOF nanosheets.[58] Zhou et al. first expanded the interlayer spacing of layered $Zn_2(PdTCPP)$ by using a chemically cleavable intercalant.[55] Then, they selectively cleaved the disulfide bonds in the intercalant using trimethylphosphine, thereby easily exfoliating ultrathin MOF nanosheets. This method, which combines intercalation with chemical exfoliation, offers a wide range of control, high yield of MOF nanosheets, and an ultrathin thickness of merely 1 nm. The researchers also controlled the thickness of the exfoliated $Zn_2(PdTCPP)$ by regulating the quantity of trimethylphosphine and the duration of the reaction. Logelin et al.[56] described an approach for the mechanical exfoliation of 2D Zn-MOFs by selectively degrading the dianthraquinone (diAn) ligands in three-dimensional (3D) Zn-MOFs through postsynthetic modification. Firstly, macroscopic crystals that can be mechanically exfoliated are synthesized by selectively reducing the dimensionality of the diAn ligands in 3D Zn-MOFs. Subsequently, through postsynthetic annealing treatment, the diAn ligands are capable of undergoing selective depolymerization, thereby achieving dimensional reduction from 3D MOFs to 2D MOFs. As-prepared 2D MOFs will subsequently be mechanically delaminated into thinner sheets. The nanosheets obtained by this method have a thickness of only 10 nm, with lateral dimensions at the micrometer level (Fig. 3f). This method not only enhances the crystallinity of the material, but also provides a possibility for preparing large-sized 2D materials with specific interlayer arrangements.

To sum up, top-down approaches have been recognized as straightforward and dependable methods. Despite the development of many mature and reliable technologies, there are still obstacles hindering their further application. The top-down approach is typically applicable only to layered MOF structures, and layered structures are prone to being damaged during exfoliation, resulting in low yield of the method, which limits its application in large-scale production. Secondly, this method typically requires a significant amount of energy, which can pose a challenge in energy-intensive industrial production, and it remains difficult to achieve precise regulation of nanosheet thickness through the modulation of external driving forces.

Thirdly, the 2D MOF nanosheets obtained by exfoliation have issues with re-stacking or structural collapse. Consequently, additional research and development are required to address the challenges associated with the top-down approach.

Bottom-up methods

Bottom-up techniques involve the assembly of molecular building blocks to create well-defined 2D structures. These approaches enable meticulous regulation of the final product's structure, composition, and functionality. The bottom-up techniques include interfacial synthesis, surfactant-assisted methods, and so on. By selecting organic linker ligands and metal sites, the characteristics of 2D MOFs can be customized to suit the demands of efficient electrocatalytic applications. The bottom-up method facilitates the production of high-quality, uniform MOF nanosheets, and has potential scalability suitable for commercial applications.

Interfacial synthesis method

The interfacial preparation approach has risen to prominence as a powerful technique for the growth of MOF nanosheets. This strategy exploits the coordination bonds formed between organic ligands and metal nodes at the boundary where two different phases meet, thereby facilitating the controlled formation of nanosheets.[59,60] The liquid–liquid and gas–liquid interfaces serve as two primary types utilized in this synthesis approach, each offering unique advantages for the production of ultrathin or even monolayer MOF nanosheets.[19,61] The gas–liquid interfacial synthesis approach is particularly effective for generating ultrathin or monolayer MOF nanosheets. The procedure commences by applying a minimal amount of a volatile organic solvent, which contains a restricted concentration of metal ions or organic ligands, onto the surface of a liquid. Once the organic solvent has completely evaporated, a gas–liquid interface is established. The evenly dispersed organic ligands or metal ions on the liquid surface promote the formation of ultrathin nanosheets at this interface. Kitagawa et al. pioneered the use of the gas–liquid interfacial fabrication approach to synthesize CoTCPP-pyridine-Cu, which has since gained widespread attention for the formation of various MOF nanosheets.[17] For instance, Nishihara and colleagues reported the preparation of ultra-thin Ni-BHT (BHT = benzenehexathiol) nanosheets using this method.[62] In their study, an ethyl acetate solution with BHT ligands was carefully applied onto the surface of an aqueous solution of $Ni(OAc)_2$. Following the evaporation of ethyl acetate, MOF nanosheets were formed at the interface (Fig. 4d). These MOF nanosheets were then placed on an aligned pyrolytic graphite (HOPG) substrate. The topological imaging displayed by scanning tunneling microscopy (STM) demonstrates that the height of the prepared Ni-BHT nanosheets was merely 0.6 nm, indicating the remarkable thinness achievable through this method (Fig. 4e and f).

The liquid–liquid interfacial synthesis approach involves the reaction between metal ions and organic ligands at the interface with two incompatible liquids. This approach has been used to produce 2D MOFs with controlled thicknesses. For instance,
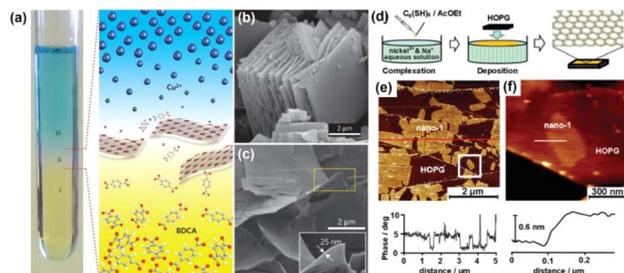
Fig. 4 (a) Diagrammatic representation of the three-layer preparation method. The figure depicts the spatial arrangement of the (i) BDC layer, (ii) middle layer and (iii) Cu^{2+} layer. SEM images of (b) bulk-type Cu-BDC MOF materials, and (c) Cu-BDC prepared by the three-layer method. Inset: a single Cu-BDC sheet with a thickness of 25 nm.[10] (d) Schematic diagram of the formation of nanosheets at the gas–liquid interface. (e) AFM image of MOF nanosheets deposited on HOPG, along with the height obtained along the trajectory of the red line. (f) AFM topographical image of a monolayer MOF nanosheet and the height profile.[62]

previously, Gascon and colleagues synthesized Cu-BDC nanosheets using a three-layer preparation method.[10] As shown in Fig. 4a, the synthesized medium was mainly composed of acetonitrile and DMF mixtures with different proportions. Since acetonitrile was less dense and DMF was denser, the vertical alignment formed three liquid layers. High concentrations of acetonitrile and DMF were dispersed at the top and bottom, respectively, and the concentrations of acetonitrile and DMF in the middle medium were equal. Since the metal ions (Cu^{2+}) were readily soluble in acetonitrile and the organic ligand (H_2BDC) was readily soluble in DMF, the top solution had a high concentration of Cu^{2+}, the bottom solution had a high concentration of H_2BDC, and the medial layer acted as a buffer layer slowing the diffusion rate of ions and ligands, resulting in the generation of thin square Cu-BDC nanosheets (Fig. 4b). The thickness of the prepared square Cu-BDC ranged from 5 to 25 nm, while its lateral dimension was approximately 0.5 to 4 μm (Fig. 4b and c). Importantly, the interlayer effectively prevented the overgrowth of Cu-BDC, and the formed nanosheets could be precipitated from the medial interface naturally. So this three-liquid layer synthesis method can effectively solve the low yield of MOF nanosheets caused by the limitation of the interfacial area. This technique offers a flexible framework for producing MOF nanosheets with adjustable properties, making it a valuable asset in the advancement of materials for various utilizations.

Surfactant-assisted method

In the preparation of nanomaterials, surfactants are frequently employed to achieve desirable morphologies or structures, as they can adhere to specific facets of nanocrystals selectively, thereby limiting extension in particular directions. Zhang et al.[63] indicated that ultrathin MOF nanosheets can be produced through a straightforward solvothermal process, aided by polyvinylpyrrolidone (PVP). The PVP molecules adhered to the Zn-TCPP surface selectively, thereby limiting the growth in the vertical direction. This selective attachment

resulted in anisotropic crystal growth, which ultimately led to the creation of extremely thin Zn-TCPP sheets. Additionally, PVP played a role in stabilizing the resulting nanosheets. Conversely, in the absence of PVP, isotropic crystal growth occurred, yielding bulk MOFs instead. A range of 2D MOFs, including M-TCPP, M-TCPP(Fe) (where M represents Zn, Cu, Co or Cd), $Cu(HBTC)(H_2O)_3$, and others, can be synthesized using the PVP-assisted method. Cetyltrimethylammonium bromide (CTAB), a commonly used surfactant, is also capable of being utilized to create MOF nanosheets.[64] Lately, Tsapatsis and colleagues found that the reaction temperature has a substantial influence on the morphology of Zn(Bim)OAc when CTAB is present.[65] In Zn(Bim)OAc, the Zn-OAc-Zn bonds were oriented along the c axis, whereas the Zn-Bim-Zn bonds were aligned along the b axis. And the Zn(Bim)OAc nanosheets were produced at 25 °C. This disparity in morphology was ascribed to the varying reaction velocity between metal nodes and organic linkers. The reaction between Zn^{2+} and Bim occurred more rapidly than that between Zn^{2+} and OAc at 110 °C, which promoted extension along the b-axis, resulting in the formation of nanobelts. Conversely, at 25 °C, the rate of reaction between Zn^{2+} and Bim decreased and became similar to that between Zn^{2+} and OAc, leading to the formation of nanosheets. Notably, recent studies have shown that nonlamellar Al-MOFs with nanosheet structures can be synthesized using an approach assisted by CTAB.

In addition to CTAB and PVP, other surfactants such as sodium dodecyl sulfate and sodium lauryl sulfate have also been documented in the production of 2D MOFs.[66,67] Certain small capping molecules, such as trifluoroacetic acid, formic acid and pyridine-often termed as regulators, can likewise be utilized in the synthesis of 2D MOFs. These small capping molecules can competitively bind to metal nodes like surfactants, thereby obstructing the extension of MOFs in certain directions and enabling the growth of MOF nanosheets. Lin and colleagues utilized formic acid as a regulator to fabricate a Hf-based 2D MOF. The six coordination sites of the Hf6 cluster were bound by formate, which inhibited growth in the vertical direction.[68] Meanwhile, the six unused coordination sites of the Hf6 cluster within the identical plane were linked by benzene-1,3,5-tribenzoate (BTB), forming a 2D structure. In essence, small capping molecules and surfactants have demonstrated significant potential in the creation of 2D MOFs. Nevertheless, they adhere to the resulting MOF nanosheets and inevitably cover some active sites, which is detrimental to electrochemical performance. Thus, from the standpoint of electrocatalytic activity, it is ideal to produce MOF nanosheets with relatively unblemished surfaces.

2D MOF nanosheets in electrocatalysis

In the preceding decades, substantial research has been focused on creating highly active catalysts for the electrochemical reaction. Certain noble metals and their oxides can be used as catalysts or traditional electrode materials. However, they are plagued by issues such as shortage, expensiveness and poor endurance. MOFs are regarded as extremely promising for

electrocatalysis, thanks to their structural tunability and high specific surface area. Among them, the surface of the MOF nanosheets can provide a multitude of active sites for the adsorption and conversion of reaction intermediates, and the unique framework structure provides a greater possibility for the contact between active sites and reactants, which is beneficial to improve the electrocatalytic reaction. The structural features of 2D MOFs overcome the problems of slow mass transfer and charge transfer in traditional bulk MOFs in electrocatalysis. Therefore, 2D MOFs have attracted considerable interest from numerous academics in the domain of electrocatalysis. Researchers have made a lot of important progress in the controllable preparation and electrocatalytic utilization of 2D MOFs, proving the feasibility of 2D MOFs and their potential application prospects.

Oxygen evolution reaction

The oxygen evolution reaction (OER) is a vital process in electrochemical water dissociation technology. Yet, the kinetics of the OER is slow and experiences high overpotential through multi electron processes. Therefore, highly active electrocatalysts with rapid electron transfer are crucial for minimizing overpotential in the OER.[69–71] Compared to precious metal catalysts (RuO_2/IrO_2) with excellent catalytic activity but high cost, the advancement of non-noble metal catalytic materials has become the mainstream trend, and therefore 2D MOF nanosheet materials have gradually become a potential stock for OER catalysts.[72,73] Defect engineering supplies a productive means for the formulation and optimization of catalysts, and by rationally introducing and modulating defects, the performance of the catalysts can be significantly enhanced. Due to the high surface energy, ultrathin nanosheets are prone to surface atom or ion migration, leading to the formation of abundant defects. Researchers have utilized this characteristic to develop a variety of ultrathin nanosheet structures for catalytic reactions, such as the ultrathin 2D FeCoNi-MOF nanosheets constructed with a thickness of only 1.5 nm.[74] The abundant oxygen vacancies formed can enhance the activation and adsorption of active oxygen on the surface of catalytic materials (Fig. 5a). Moreover, the oxygen vacancies were dynamically evolved during the reaction process, which greatly improved the catalyst lifespan, allowing stable catalysis for over 100 hours in alkaline electrolyte (Fig. 5c). Additionally, the large surface free energy of the ultrathin nanosheets caused them to exhibit a highly curved state, which facilitated the reaction of more edge active sites, thus demonstrating excellent catalytic performance. This resulted in a reduced overpotential (254 mV) at 10 mA cm^{-2} (Fig. 5b).

Apart from defect engineering, surface modification can also significantly improve the electrocatalytic efficiency of 2D MOF nanosheets. Song et al.[75] grew NiFe-MOF nanosheets in situ on carboxylated carbon quantum dots (CQDs-COOH), avoiding the complex thermal decomposition at high temperatures and effectively preserving the inherent structural diversity of the material. CQDs-COOH expanded the interlayer spacing between nanosheets during the synthesis of NiFe-MOF, and utilized the electron-attracting ability of –COOH to modulate the electronic configuration around the metal active sites, enhancing the
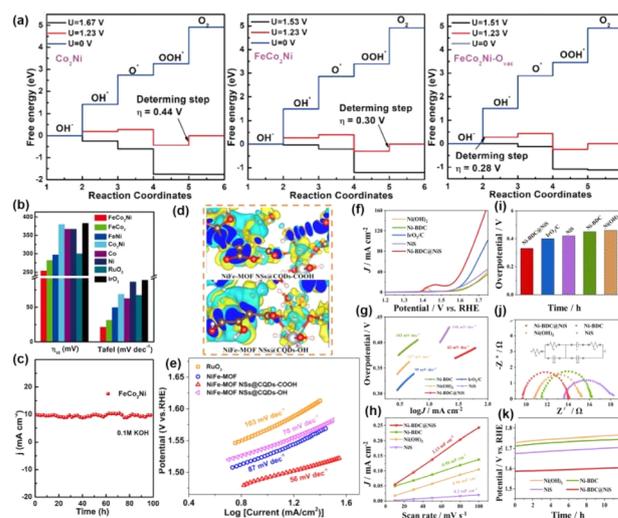

Fig. 5 (a) The free-energy diagrams of Co_2Ni-MOF-74, $FeCo_2NiMOF$-74 and $FeCo_2Ni$-MOF-74. (b) Comparison of the Tafel slope and overpotential of precious metal oxides and the MOF materials in this work. (c) The stability measurements for $FeCo_2Ni$-MOF-74.[74] (d) The difference charge density of catalysts. Yellow indicates a decrease in electron density, while blue signifies an increase. (e) Tafel plots of catalysts.[75] (f–k) The electrochemical performance of the Ni-BDC@NiS comparison sample.[76]

positive charge density, which enhanced the catalytic performance in the OER (Fig. 5d). This NiFe-MOF@CQDs-COOH composite catalyst exhibited a small Tafel slope and the overpotential in 1 M potassium hydroxide (KOH) electrolyte was 261 mV. Its durability was demonstrated after testing for a long period of 48 hours (Fig. 5e).

Doping is also a method of surface modification, and in the formulation of MOF-based electrocatalysts, it mainly involves incorporating metals to conduct multi-site synergistic catalysis. Moreover, the introduced metals can proficiently modulate the construction of the electronic configuration and defects on the surface of catalytic materials.[77,78] For instance, the single-metal MOF materials have issues such as insufficient activity, high overpotential, and limited reaction kinetics in OER applications under acidic conditions. Liu et al.[79] constructed 2D bimetallic MOF nanosheets ($Ni_{0.6}Co_{0.4}$-MOF NSs), and both Co and Ni participated in the construction process of the 2D MOF nanosheets. Moreover, compared to single-metal MOF materials, the incorporation of Co in the construction of $Ni_{0.6}Co_{0.4}$-MOF NSs altered the electronic milieu around the active centers on the surface of $Ni_{0.6}Co_{0.4}$-MOF NSs. The migration of electrons around Co and the accumulation of electron clouds around Ni sites led to the reconstruction of some orbital electrons and a decrease in binding energy. The synergistic interaction between Co and Ni metal sites facilitates the excitation or participation of electrons in electrochemical reaction processes, enhancing the inherent activity of $Ni_{0.6}Co_{0.4}$-MOF NSs.

Incorporating conductive materials, like carbon black, to construct composite catalysts further improves the OER performance. Zhang et al.[80] precisely replaced Ni^{2+} sites in Ni-MOF with Fe, creating abundant oxygen vacancies and

keeping the catalyst surface in a highly oxidized state (Ni^{3+}/ Ni^{4+}), which kept the Ni active sites in a favorable dynamic conversion state. This promoted the electron migration process and enhanced the durability of the catalyst. At the same time, researchers constructed a composite catalyst with a heterostructure of Fe-doped $Ni_{0.67}Fe_{0.33}$-MOF and carbon fiber paper (CFP), which was applied to the OER and exhibited an ultrafast electrochemical reaction rate (38 mV dec^{-1}). Thus, the construction of heterogeneous structures is also an efficient and popular method for catalyst design. This method can compensate for the drawbacks of the unstable structure and weak conductivity in 2D MOF nanosheets. For example, the composite catalyst (ZIF-9(III)/Co-LDH) designed and constructed by Chen et al.,[81] which combines Co-LDH and 2D ZIF-9, is similar to porous materials and possesses a large specific surface area. This facilitates the enrichment of reactive substances and exposes more active centers, significantly improving the active specific surface area of ZIF-9(III)/Co-LDH. Specifically, the heterogeneous interface between Co-LDH and 2D ZIF-9 not only expedited electron migration but also aided in the activation and migration of reactive species. The electrochemical performance of this composite catalyst was not only significantly superior to that of its individual components but also surpasses that of commercial precious metal oxide catalysts.

Compared to a composite of two materials, the catalyst obtained by in situ construction of the heterostructure is more stable. He et al. conducted in situ partial sulfidation on $[Ni_3(OH)_2(1,4\text{-}BDC)_2(H_2O)_4]\cdot 2H_2O$ nanosheets, for preparing the Ni-BDC@NiS composite layered catalyst.[76] The construction of this in situ heterostructure not only enhanced the structural integrity, but the partial sulfidation of Ni sites also altered the electron cloud density around them, which was beneficial for water adsorption and the enrichment of active substances (Fig. 5f–k). The channels formed by the nanosheet arrays facilitated rapid mass transfer, and the high conductivity of NiS was also one of the key reasons for enhancing the electrocatalytic activity. Ni et al.[82] combined defect engineering with the construction of heterogeneous structures, preparing γ-FeOOH/ Ni-MOFNA nanosheet array catalytic materials based on MOF materials by introducing connector defects. The Ni/Fe dual active sites constructed at the heterojunction interface had efficient oxygen evolution capability, and the overpotential of this catalyst at 10 mA cm^{-2} was significantly reduced to below 200 mV. Liu et al.[83] combined structural induction with elemental doping to conceive and prepare a 2D Co-based MOF. Researchers first achieved the reassembly from 3D to 2D structures through the replacement of organic ligands, and then introduced Fe to improve the electronic architecture around the Co centers, promoting the adsorption and evolution of active oxygen species. These research efforts provide many new references for the design of highly active MOF nanosheets.

Hydrogen evolution reaction

With increasing concerns about fuel shortages and CO_2 emissions, hydrogen is considered an ideal substitute for fossil fuels as an energy carrier. Although precious metals like Pt currently remain the most effective catalysts for the HER,[84,85] in recent years, 2D MOFs and their derivatives as a class of low-cost and efficient HER electrocatalysts have attracted extensive attention in the academic community, and a lot of important progress have been made.[86–88] Huang et al.[89] presented that a bimetallic site conductive MOF ($M_3(M_3HAHATN)_2$) featuring an additional M–N_2 moiety was prepared by using hexaiminohexaazatrinaphthalene (HAHATN) as the conjugated ligand. The obtained $Ni_3(Ni_3\cdot HAHATN)_2$ nanosheets consisted of a smooth, silk-like layered structure, and the average thickness was 1.6 nm (Fig. 6a and b). The crystal structure analysis of the $Ni_3(Ni_3\cdot HAHATN)_2$ nanosheets revealed that a regular hexagonal ring, formed by six $Ni_3HAHATN$ units linked via Ni–N_4 bonds, constitutes a 2D MOF, which exhibited an enlarged mesoporous structure (pore size of 2.7 nm). The large structure with enlarged in-plane pores can facilitate mass diffusion for small molecules within the framework, and the unsaturated metal atoms in the M_1–N_2 moiety were the main active sites. The HER onset potential of $Ni_3(Ni_3HAHATN)_2$ was 12 mV, lower than that of $Ni_3(HITP)_2$ (51 mV) (Fig. 6c and d). Zhu and colleagues[90] synthesized the 2D Co-BDC/MoS_2 nanosheets by the ultrasound approach. The coupling of Co-BDC to MoS_2 triggered a partial phase transition from 2H-MoS_2 to 1T-MoS_2. On increasing the electrical conductivity, more catalytically active sites were exposed, thus enhancing the catalytic efficiency for the HER. 2D Co-BDC/MoS_2 required an overpotential of 155 mV to reach a current density of 10 mA cm^{-2}, which was less than that of MoS_2 (349 mV) and Co-BDC (529 mV) (Fig. 6e and f). Rui et al.[92] synthesized 2D Ni-MOF@Pt by realizing in situ formation of Pt nanoparticles on 2D Ni-MOF. The 2D Ni-MOF nanosheets were uniformly decorated with Pt nanoparticles, which had an average size of approximately 3.23 nm. The synthesized 2D Ni-MOF@Pt demonstrated effective catalytic efficiency for the HER in both acidic and alkaline electrolytes. In acid solution, 2D Ni-MOF@Pt showed a low overpotential (43 mV) and the Tafel slope was 30 mV dec^{-1} at 10 mA cm^{-2}. In alkaline electrolyte, 2D Ni-MOF@Pt exhibited a desirable electrocatalytic performance, achieving an overpotential of 102 mV. The improvement of catalytic capability of 2D Ni-MOF@Pt can be
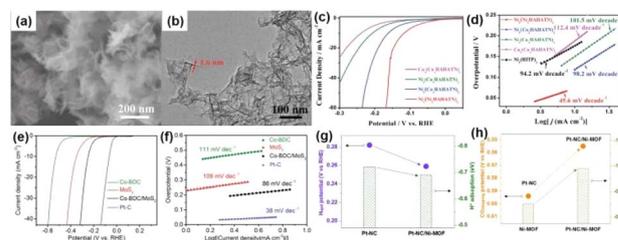

Fig. 6 (a) SEM image and (b) TEM image of $Ni_3(Ni_3\cdot HAHATN)_2$ nanosheets. (c) LSV plots of $M2_3(M1_3\cdot HAHATN)_2$ and (d) Tafel plots.[89] (e) The polarization curves of MoS_2, Co-BDC and Co-BDC/MoS_2 and so on. (f) Tafel plots of catalysts.[90] (g) Graphs showing the Hupd desorption peak potentials derived from cyclic voltammetry (CV) plots, as well as the H* adsorption energy predicted through density functional theory (DFT) calculation. (h) Graph of CO stripping peak potentials.[91]

primarily ascribed to the following points: (1) the abundant Pt–O bonds enhanced the activity of the Pt active center; (2) the rearrangement of the charge density led to the improved conductivity of the interface; (3) the Ni-compressive strain induced by the strong interfacial interactions in Ni-MOF@Pt heterostructures. Guo *et al.*[91] prepared Pt-NC/Ni-MOF by sonicating commercial Pt on carbon black (Pt-NC) with Ni-MOF nanosheets synthesized by combining nickel salts with benzenedicarboxylic acid ligands in an aqueous solution. At an overpotential of 50 mV, the catalyst achieved a current density of 21.7 mA cm^{-2} for the HER. This value was twice that of Pt-NC and 1.6 times higher than that of Pt-NC/Ni(OH)$_2$. The mass activity of Pt-NC/Ni-MOF reached 7.92 mA μg_{Pt}^{-1} at an overpotential of 70 mV, which was 1.96 and 2.53 times higher than that for Pt-NC/Ni(OH)$_2$ and Pt-NC, respectively(Fig. 6g and h).

Oxygen reduction reaction

The oxygen reduction reaction (ORR) occurs at the cathode of the fuel cell, where oxygen is reduced to form water molecules, and MOFs provide a framework with a large surface area and metal centers. The extensive surface area facilitates easy availability for O$_2$ molecules, while the metal sites form the foundation for catalytic reactions. Introducing defects, increasing edge active centers, and promoting electron transfer are common strategies to enhance the performance of electrocatalysts, especially for MOF-based catalysts with poor conductivity. Therefore, defect engineering is also very common in the design of ORR catalysts. Yang *et al.*[93] created defects by removing some imidazole linkers and developed Co/Zn-ZIF nanosheet arrays with high ORR activity. The difference between the OER and ORR lies in the amount of electron transfer (Fig. 7a and b), and how to balance the adsorption energy of active oxygen species to achieve efficient OER and ORR catalysis is a key issue in catalyst design. The construction of dual active sites provides a possible solution to this. Cheng *et al.*[94] synthesized bimetallic NiMn-MOF on porous carbon fibers using the solvothermal method and organic ligand-induced exchange method. Ni served as the main active center, and the coordination defects caused by the addition of Mn created abundant free electrons, which were conducive to the generation of critical reaction intermediates *O and *OOH. The combined action of Ni and Mn significantly accelerated the reaction kinetics of the OER and ORR (Fig. 7c and d).

Nowadays, MOF-based composite derivatives have shown excellent performance in the ORR, but the design of such catalysts still requires precise control over pyrolysis conditions to optimize the structure and composition, thereby achieving efficient electrocatalytic performance and stability. As an example, Huang *et al.*[95] designed a 2D MOF nanosheet coupled array (R-NCM) through a growth-heat treatment-regrowth strategy (Fig. 7e). In R-NCM, some metal Ni and Co nodes were reduced to metal atoms (Fig. 7f), and there were phases of metal Ni, Co, and C present, which can help to promote charge transfer. At the same time, this MOF composite nanoarray was binder-free, structurally stable, and has a high electrochemically active surface area (Fig. 7g). The conductivity of catalysts
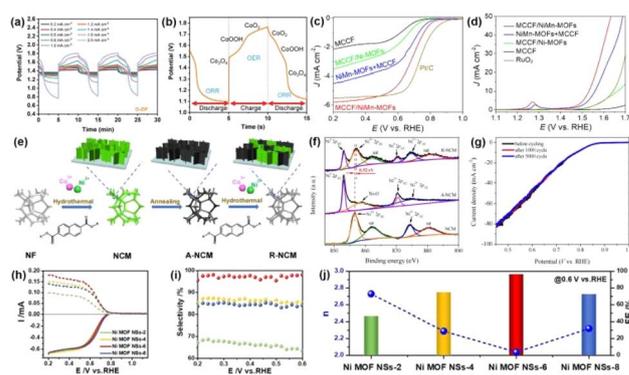

Fig. 7 (a) Electrochemical discharge−charge characteristics of D-ZIF-ZABs at different current densities. (b) The voltage plots of the charge−discharge cycles.[93] (c) LSV curves at 1600 (rpm) for ORR performance. (d) LSV plots obtained in 1 M KOH for OER performance.[94] (e) Schematic diagram of the growth-pyrolysis-regrowth process on a Ni foam substrate. (f) The XPS spectra of Ni 2p. (g) The polarization curves of R-NCM before and after cycling for the ORR.[95] The ORR performance of Ni MOF NSs. (h) Polarization plots and simultaneous H$_2$O$_2$ detection currents. (i) H$_2$O$_2$ selectivity determined through RRDE experiments. (j) The quantity of electrons transferred and the corresponding FE.[96]

can be enhanced by carbonizing MOF materials, but the structural design and construction of MOF materials before carbonization are key to MOF-based carbonized derivatives. Liu *et al.*[97] first limited the size of Co nanoparticles loaded by stripping Zn-MOF nanosheets. Subsequently, Co nanoparticle decorated ultrathin N-doped C nanosheets (Co@N-CNSs) were prepared by pyrolysis, and the half-wave potential in the ORR reached 0.89 mV. In addition, Wang *et al.*[96] utilized a liquid–liquid interface synthesis method to fabricate 2D Ni-MOF nanosheets by an adjusting the ratio of metal precursors to organic connectors (RM/L) to modulate the active sites. The Ni-MOF nanosheets with a high RM/L demonstrated an obvious dependence on the 2e ORR to hydrogen peroxide (H$_2$O$_2$). The Ni-MOF nanosheets demonstrated the best near-zero overpotential at an RM/L of 6, with an H$_2$O$_2$ selectivity of approximately 98% and a yield of approximately 80 mmol g$_{cat}^{-1}$ h^{-1} (Fig. 7h–j).

The ligands surrounding the active site transitioned from saturated to unsaturated and partially unsaturated metal centers were crucial for forming the ideal site to boost electrocatalysis. Wang *et al.*[98] demonstrated a dual-site coupling evolution in the pyrolytic synthesis of MOF-derived catalysts, that is, the synergistic effect of metal sites and single-atom metal sites. These catalysts with monoatomic metal sites showed no decrease in activity in the ORR after complete removal of the metallic cobalt sites.

CO$_2$ reduction reaction

Transforming CO$_2$ into invaluable chemicals and fuels represents a practical approach for addressing the challenges of energy scarcity and climate change.[99–102] Nevertheless, the direct transformation of CO$_2$ necessitates substantial energy expenditure, attributed to its considerable chemical stability. One prospective method for CO$_2$ conversion is through its

electrocatalytic reduction. Electrocatalysts for the CO_2RR have gradually become a research hotspot. Among them, 2D MOF nanosheets have gradually entered the field of researchers' vision.[103] Tian et al. explored the application of 2D π-conjugated metal bis(dithiolene) nanosheets as promising electrocatalysts for the CO_2RR.[104] Researchers utilized DFT calculations to predict the CO_2RR catalytic activity of different metals in $M_3C_{12}S_{12}$ (M = Co, Fe, Ni, Rh, Ru and Pd) structures (Fig. 8a). Experimental results consistent with theoretical calculations indicate that Ru and Rh, as metal centers, exhibit low free energy barriers, making them potential CO_2RR electrocatalysts. Furthermore, researchers have clarified the reaction pathway for CH_4 production, where the generation of *CHO serves as the rate-limiting step (Fig. 8b). Therefore, the selection and regulation of the metal center are key to achieving efficient catalysis.

Although MOF materials have become a promising material for CO_2RR electrodes on account of their large CO_2 adsorption capacity and abundant adjustable active sites, their insulation often leads to low current density. Thus, Zhang et al.[105] introduced a 2D MOF nanosheet material based on nickel phthalocyanine (NiPc-Ni(NH)₄), which achieves high electrical conductivity through the convergence between Ni nodes and NiPc groups to form d–π conjugated orbitals, demonstrating excellent catalytic performance in the CO_2RR. The main active center of NiPc-Ni(NH)₄ is the NiPc group, and the primary outputs are CO and H_2 within a fixed voltage range, reaching the highest faradaic efficiency (FE) of CO (96.4%) at a potential of −0.7 V (vs. RHE) (Fig. 8c and d). According to theoretical calculation results, the NiPc group is more favorable for the generation of *COOH, so the HER is not severe at lower potentials. Yi and colleagues synthesized conductive 2D phthalocyanine-based MOF nanosheets ($NiPc-NiO_4$) interconnected by nickel-catecholate bonds. These nanosheets serve as high-performance catalysts for the CO_2RR to CO. The synthesized 2D $NiPc-NiO_4$ possesses outstanding electrical conductivity. They achieve a remarkable selectivity of 98.4% for CO, along with a notable partial current density of 34.5 mA cm^{-2} (Fig. 8e and f), surpassing the activity of previously reported MOF catalysts.[106] The Bi-MOF designed by Huang et al.[107] was reconstructed into ultra-thin $Bi_2O_2CO_3$ nanosheets during the electrolysis process. The reconfigured $Bi_2O_2CO_3$ nanosheets reveal a crystalline surface structure that lowers the activation energy threshold for the electrochemical CO_2RR intermediate *OCHO and stabilizes *OCHO (Fig. 8g). In consequence, this structure is more advantageous for enhancing the selectivity of the electrochemical CO_2RR towards formate formation. As shown in Fig. 8h and i, the FE for formate can reach 96% with a CO_2RR current density of 25 mA cm^{-2} when the voltage was set at −0.9 V (vs. RHE). Bi-BTC also demonstrates excellent electrochemical stability, maintaining $FE_{formate}$ and current density for 24 hours with virtually no decline.

Other electrocatalytic reactions

The electrocatalytic glycerol oxidation reaction (GOR) is emerging as a cost-effective and promising technological alternative to the OER for the co-production of valuable chemicals and H_2. Optimizing the interaction between glycerol (GLY) and hydroxyl (OH) groups is essential for improving the efficiency of the GOR. Zhao et al. developed a hierarchical p–n heterojunction structure by combining Co-MOF nanosheets with CuO nanorod arrays, creating a (CuO@Co-MOF) composite to enhance the performance of the GOR (Fig. 9a).[108] In particular, the CuO@Co-MOF electrode demonstrated remarkable performance, achieving a conversion efficiency of 98.4%, a selectivity for formic acid (FA) of 87.3%, and a FE of 98.9% (Fig. 9b and c). When utilized in a flow-cell system for coupling the GOR with the HER, the bifunctional CuO@Co-MOF electrode exhibited enhanced energy conversion efficiency. The introduction of Co-MOF not only caused a redistribution of the surface electric field and enhanced OH adsorption, but also regulated the excessive GLY adsorption of CuO, thereby reducing the reaction energy barrier for FA desorption. Meanwhile, the architecture is capable of enhancing the concentration of hydroxide ions (OH^-) and facilitating their mass transfer within the solution.

The electrocatalytic nitrate reduction reaction (NO_3^-RR) is an important route for sustainable NH_3 synthesis and environmental remediation. Zou et al.[109] fabricated a MOF-on-MOF heterostructured electrocatalyst with interfacial dual active sites and a built-in electric field for efficient NO_3^-RR for NH_3 production. By growing Co-HHTP nanorods on Ni-BDC nanosheets, the generation of Ni–O–Co bonds at the interface of the MOF-on-MOF heterostructure led to dual active sites for NO_3^-RR. The Ni sites facilitated the activation and surface binding of NO_3^-, while the Co centers boosted H_2O decomposition to supply active hydrogen (H_{ads}) for the hydrogenation of N-containing intermediates on adjacent Ni sites, cooperatively reducing the energy barriers of the NO_3^-RR process. Together
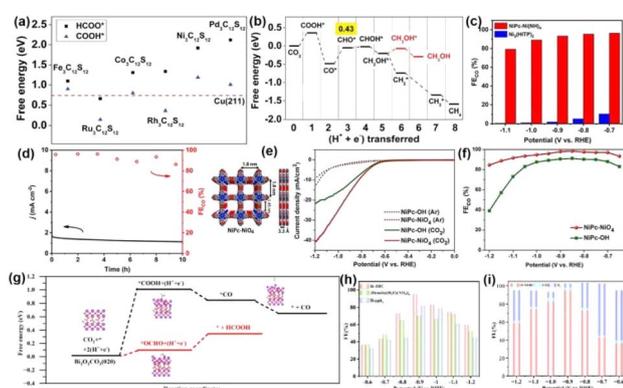

Fig. 8 (a) The free energy required for the generation of HCOO* and COOH* on a monolayer $M_3C_{12}S_{12}$ sheet. The red dashed line indicates that the threshold for determining catalytic activity is set at $\Delta G < 0.74$ eV. (b) The free energy of the CO_2RR on $Rh_3C_{12}S_{12}$.[104] (c) The FE_{CO} from −0.7 to −1.1 V. (d) The stability assessment of NiPc-Ni(NH)₄.[105] (e) Top and side views of a catalyst arranged in a 2 × 2 square grid with an AA-stacking configuration, and LSV curves of the catalysts. (f) The FE_{CO} of $NiPc-NiO_4$ and NiPc-OH.[106] (g) Free energy diagram for the CO_2RR on $Bi_2O_2CO_3$. (h) $FE_{formate}$ of Bi-BTC, Bipph₃, and [Bi(mela)(H_2O)NO_3]$_n$. (i) Distribution of electrolytic products from the Bi-BTC electrocatalyst and their corresponding FE at various potentials.[107]
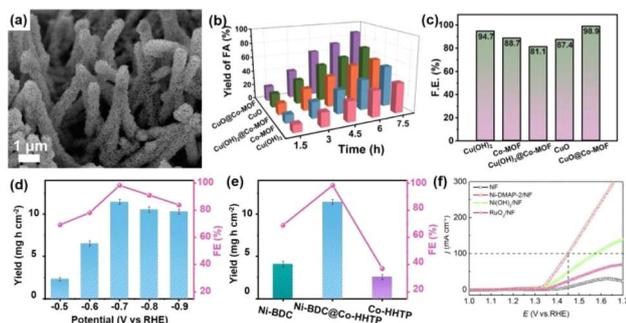
Fig. 9 (a) SEM image of CuO@Co-MOF. (b) Yield for FA production. (c) The FE for FA production at 1.43 V on different catalysts.[108] (d) The FE_{NH_3} and NH_3 yield rate of Ni-BDC@Co-HHTP at different voltages. (e) The FE_{NH_3} and NH_3 yield rate of different catalysts.[109] (f) The LSV curves of catalysts.[110]

with the accelerated electron transfer enabled by the built-in electric field, a remarkable NO_3^-RR performance was achieved with an NH_3 yield rate of 11.5 mg h^{-1} cm^{-2} and a FE of 98.4% (Fig. 9d and e), outperforming most reported MOF-based electrocatalysts. The activity of Ni-based catalysts in the UOR was significantly influenced by the availability of Ni centers exposed in the course of the electrochemical reaction.[111] The rapid charge transfer properties and high concentration of Ni centers on the surface of nanosheets were beneficial to improve the UOR performance of Ni-based MOF.[112,113] Jiang and colleagues[110] prepared Ni-DMAP-2/NF on nickel foam by a one-step solvothermal method, employing $Ni(NO_3)_2$ and 4-dimethylaminopyridine (DMAP) as metal precursors and organic linkers, respectively. Ni-DMAP-2 exhibited a characteristic structure of interconnected nanosheets with lateral dimensions spanning several hundred nanometers, and the thickness of Ni-DMAP-2 was about 3.7–3.9 nm. As shown in Fig. 9f, the overpotential of Ni-DMAP-2 was 1.45 V (*vs.* RHE) at a current density of 100 mA cm^{-2}. Wang and his group[114] fabricated 2D Ni_2P@Ni-MOF/NF by embedding Ni_2P nanocrystals into Ni(BDC)(DMF) *via* a direct phosphating process. To reach a current density of 100 mA cm^{-2} for the UOR, a voltage of 1.41 V was required. Among the various catalysts tested, Ni_2P@Ni-MOF/NF demonstrated the smallest Tafel slope, amounting to 43.8 mV dec^{-1}. This value was lower than those of Ni_2P@NiC/NF, NiC/NF and Ni-MOF/NF, indicating superior electrocatalytic kinetics.

Conclusions and perspectives

This review systematically summarizes the preparation strategies for 2D MOF nanosheets, as well as the regulation of their activity and application. The main synthesis methods of MOF nanosheets include bottom-up and top-down approaches. We mainly introduce some synthesis methods such as physical exfoliation and chemical exfoliation, and discuss their principles and effects. In addition, we summarized the employment of 2D MOFs in electrocatalysis in the last few years. Obviously, 2D MOFs have great development potential due to their unique structural advantages, but the current research studies still have

certain shortcomings and scientific challenges that need to be addressed.

Current challenges in 2D MOF nanosheet research

Synthesis and scalability. The synthesis of high-quality 2D MOF nanosheets often involves complex procedures and harsh conditions, limiting their large-scale production. Developing scalable and cost-effective synthesis methods is a major challenge.

Stability under electrochemical conditions. Many 2D MOFs suffer from poor stability in electrochemical environments, leading to degradation and loss of catalytic activity. Enhancing the stability of 2D MOF nanosheets under prolonged electrocatalytic operation is crucial for practical applications.

Integration with electrode materials. Effective integration of 2D MOF nanosheets with electrode materials remains a challenge. Poor contact between the nanosheets and the electrode substrate can hinder electron transfer and reduce overall performance.

Opportunities for future research

Innovative synthesis strategies. It is very desirable to develop a simple, cost-effective and high-yield operation approach to synthesize 2D MOF nanosheets, such as green chemistry approaches or template-free synthesis, which can lead to the development of high-performance 2D MOF nanosheets with improved properties. After all, each synthetic approach has its own disadvantages and limitations. Especially for some newly developed 2D MOF structures, the synthesis methods are mostly tedious. It is one of the breakthrough points to design more suitable organic ligands and structure-oriented agents. Moreover, the development of synthesis methods suitable for the same series of 2D MOF nanosheet structures also remains a key research focus.

Hybrid materials and composites. Combining 2D MOF nanosheets with other materials, such as conductive polymers or carbon-based materials, can enhance their stability and conductivity, thereby expanding their applications in electrocatalysis. Meanwhile, the MOF nanosheets have great potential in the domain of catalytic chemistry on account of their large active specific surface area. Nevertheless, the regulation of surface-active sites (*e.g.*, acid sites and electronic properties) has not been sufficiently studied, and the electroconductibility of 2D MOFs cannot fulfill the requirements.

Advanced characterization techniques. In the current research, the characterization of the surface structure of 2D MOFs is not enough. The theoretical calculation and *in situ* characterization can be used to study the adsorption or reaction conversion pathway on 2D MOFs. Utilizing advanced characterization techniques, such as *in situ* spectroscopy and high-resolution microscopy, can provide deeper insights into the structure–property relationships of 2D MOFs, guiding their rational design and optimization.

All in all, there is still a lot of work to explore MOF nanosheets. Although the construction of ultra-thin 2D MOF nanosheets has not been reported a lot at present, it is believed that

in the future, 2D MOFs with atomic thickness will be developed, which will provide a great quantity of low-coordination surface atoms as catalytic activity centers, and the atomic-level thickness can achieve rapid reaction intermediate transfer and transport. These characteristics will enable further breakthroughs in the employment of MOF nanosheets in catalysis, ultra-sensitive sensing, biomedicine, and other fields.

Data availability

The data supporting this article have been included.

Author contributions

Conceptualization: P. W and Z. L; writing –original draft: P. W, C. Y, and J. Y; writing – review: P.W, H. L, and Z. H; and editing: P. W.

Conflicts of interest

There are no conflicts to declare.

Acknowledgements

Notes and references

1 M. Zhao, Y. Huang, Y. Peng, Z. Huang, Q. Ma and H. Zhang, *Chem. Soc. Rev.*, 2018, **47**, 6267–6295.

2 G. Chakraborty, I. H. Park, R. Medishetty and J. J. Vittal, *Chem. Rev.*, 2021, **121**, 3751–3891.

3 X. Wei, S. Cao, H. Xu, C. Jiang, Z. Wang, Y. Ouyang, X. Lu, F. Dai and D. Sun, *ACS Mater. Lett.*, 2022, **4**, 1991–1998.

4 C. Tan, X. Cao, X. J. Wu, Q. He, J. Yang, X. Zhang, J. Chen, W. Zhao, S. Han, G. H. Nam, M. Sindoro and H. Zhang, *Chem. Rev.*, 2017, **117**, 6225–6331.

5 K. P. Bera, G. Haider, M. Usman, P. K. Roy, H. I. Lin, Y. M. Liao, C. R. P. Inbaraj, Y. R. Liou, M. Kataria, K. L. Lu and Y. F. Chen, *Adv. Funct. Mater.*, 2018, **28**(51), 1804802.

6 H. Arora, R. Dong, T. Venanzi, J. Zscharschuch, H. Schneider, M. Helm, X. Feng, E. Canovas and A. Erbe, *Adv. Mater.*, 2020, **32**, e1907063.

7 D. Y. Ahn, D. Y. Lee, C. Y. Shin, H. T. Bui, N. K. Shrestha, L. Giebeler, Y. Y. Noh and S. H. Han, *ACS Appl. Mater. Interfaces*, 2017, **9**, 12930–12935.

8 W. Xu, J. Wang, H. Yu, P. Liu, G.-R. Zhang, H. Huang and D. Mei, *Appl. Catal., B*, 2022, **308**, 121218.

9 Y. Sun, M. Amsler, S. Goedecker, A. Caravella, M. Yoshida and M. Kato, *CrystEngComm*, 2019, **21**, 3948–3953.

10 T. Rodenas, I. Luz, G. Prieto, B. Seoane, H. Miro, A. Corma, F. Kapteijn, F. X. Llabrés i Xamena and J. Gascon, *Nat. Mater.*, 2015, **14**, 48–55.

11 S. Meng, G. Li, P. Wang, M. He, X. Sun and Z. Li, *Mater. Chem. Front.*, 2023, **7**, 806–827.

12 W. Wang, S. Song, P. Wang, M. He, Z. Fang, X. Yuan, H. Li, C. Li, X. Wang, Y. Wei, W. Song, H. Xu and Z. Li, *ACS Catal.*, 2023, **13**, 4597–4610.

13 C. Chen, J. K. Sun, Y. J. Zhang, X. D. Yang and J. Zhang, *Angew. Chem., Int. Ed.*, 2017, **56**, 14458–14462.

14 S. Hu, J. Zhang, S. Chen, J. Dai and Z. Fu, *ACS Appl. Mater. Interfaces*, 2017, **9**, 39926–39929.

15 Z. Li, J. Chu, D. Meng, Y. Wen, X. Xing, H. Miao, M. Hu, C. Yu, Z. Wei, Y. Yang and Y. Li, *ACS Catal.*, 2019, **9**, 8659–8668.

16 H.-C. Zhou, J. R. Long and O. M. Yaghi, *Chem. Rev.*, 2012, **112**, 673–674.

17 R. Makiura, S. Motoyama, Y. Umemura, H. Yamanaka, O. Sakata and H. Kitagawa, *Nat. Mater.*, 2010, **9**, 565–571.

18 F. Wang, W. Hu, S. Zhang, C. Zhu, Y. Fan and Q. Wang, *Microporous Mesoporous Mater.*, 2023, **351**, 112480.

19 R. Makiura and O. Konovalov, *Sci. Rep.*, 2013, **3**, 2506.

20 P. Z. Li, Y. Maeda and Q. Xu, *Chem. Commun.*, 2011, **47**, 8436–8438.

21 H. D. Yu, M. D. Regulacio, E. Ye and M. Y. Han, *Chem. Soc. Rev.*, 2013, **42**, 6006–6018.

22 Y. Wen, Q. Liu, S. Su, Y. Yang, X. Li, Q. L. Zhu and X. Wu, *Nanoscale*, 2020, **12**, 12767–12772.

23 D. B. Tripathy, *Desalination*, 2024, **592**, 118183.

24 H. Sun, K.-Z. Wang, M.-R. Yao, C.-X. Yu, Y.-H. Song, J. Ding, Y.-L. Zhou, D. Liu and L.-L. Liu, *Inorg. Chem. Front.*, 2023, **10**, 6566–6577.

25 B. Zhu, D. Wen, Z. Liang and R. Zou, *Coord. Chem. Rev.*, 2021, **446**, 214119.

26 A. E. Baumann, D. A. Burns, B. Liu and V. S. Thoi, *Commun. Chem.*, 2019, **2**, 86.

27 Y. Zhang, J. Wang, Y. Zhang, Q. Zheng, L. Wang and W. Jiang, *Adv. Sci.*, 2025, **12**, 2416210.

28 J. Liu, G. Xing and L. Chen, *Acc. Chem. Res.*, 2024, **57**, 1032–1045.

29 Y. Lu, P. Samori and X. Feng, *Acc. Chem. Res.*, 2024, **57**, 1985–1996.

30 Z. Wang, G. Wang, H. Qi, M. Wang, M. Wang, S. Park, H. Wang, M. Yu, U. Kaiser, A. Fery, S. Zhou, R. Dong and X. Feng, *Chem. Sci.*, 2020, **11**, 7665–7671.

31 C. Li, W. Zhang, Y. Cao, J. Y. Ji, Z. C. Li, X. Han, H. Gu, P. Braunstein and J. P. Lang, *Adv. Sci.*, 2024, **11**, e2401780.

32 Y.-X. Li, Y. Hu, H.-S. Bae, J. Du, S. Zhao, D. Pan and W. Choi, *ACS Nano*, 2024, **18**, 29233–29247.

33 I. E. Khalil, C. Xue, W. Liu, X. Li, Y. Shen, S. Li, W. Zhang and F. Huo, *Adv. Funct. Mater.*, 2021, **31**, 2010052.

34 S. Chongdar, R. Chatterjee, S. Reza, S. Pal, R. Thapa, R. Bal and A. Bhaumik, *Adv. Energy Mater.*, 2024, 2403809.

35 J. Yu, J. Xiao, L. Guo, Z. Xie, K. Wang, Y. Wang, F. Hao, Y. Ma, J. Zhou, P. Lu, G. Wang, X. Meng, Z. Zhu, Q. Li, C. Ling, J. Sun, Y. Wang, S. Song and Z. Fan, *ACS Nano*, 2024, **18**, 33602–33613.

36 J. Wang, A. Zhang, W. Niu, G. Liu, X. Zhou, L. Wang, X. Liu, L. Li, Z. Li, L. Zhai, Q. Yang, B. Huang, Q. Wa, Q. Yun, H. Cheng, Y. Ge, J. Huang, Z. Hu, B. Chen, Q. Zhang,

Z. Fan, L. Gu and H. Zhang, *Adv. Funct. Mater.*, 2024, 2405073.

37 D. Kim, W.-G. Lim, Y. Kim, L. S. Oh, S. Kim, J. H. Park, C. Jo, H. J. Kim, J. Kang, S. Lee and E. Lim, *Appl. Catal., B*, 2023, **339**, 123104.

38 D. Chen, J. Liu, J. Shen, Y. Zhang, H. Shao, C. Chen and S. Wang, *Adv. Energy Mater.*, 2024, **14**, 2303820.

39 P. Amo-Ochoa, L. Welte, R. Gonzalez-Prieto, P. J. Sanz Miguel, C. J. Gomez-Garcia, E. Mateo-Marti, S. Delgado, J. Gomez-Herrero and F. Zamora, *Chem. Commun.*, 2010, **46**, 3262–3264.

40 F. Israr, D. K. Kim, Y. Kim, S. J. Oh, K. C. Ng and W. Chun, *Ultrason. Sonochem.*, 2016, **29**, 186–193.

41 L. J. Han, D. Zheng, S. G. Chen, H. G. Zheng and J. Ma, *Small*, 2018, **14**, e1703873.

42 C. Vaitsis, G. Sourkouni and C. Argirusis, *Ultrason. Sonochem.*, 2019, **52**, 106–119.

43 A. Abhervé, S. Mañas-Valero, M. Clemente-León and E. Coronado, *Chem. Sci.*, 2015, **6**, 4665–4673.

44 Y. Peng, Y. Li, Y. Ban, H. Jin, W. Jiao, X. Liu and W. Yang, *Science*, 2014, **346**, 1356–1359.

45 L. Niu, J. N. Coleman, H. Zhang, H. Shin, M. Chhowalla and Z. Zheng, *Small*, 2016, **12**, 272–293.

46 P. Chandrasekhar, A. Mukhopadhyay, G. Savitha and J. N. Moorthy, *J. Mater. Chem. A*, 2017, **5**, 5402–5412.

47 G. Hai, X. Jia, K. Zhang, X. Liu, Z. Wu and G. Wang, *Nano Energy*, 2018, **44**, 345–352.

48 C. Li, X. Hu, W. Tong, W. Yan, X. Lou, M. Shen and B. Hu, *ACS Appl. Mater. Interfaces*, 2017, **9**, 29829–29838.

49 Z.-Q. Li, L.-G. Qiu, T. Xu, Y. Wu, W. Wang, Z.-Y. Wu and X. Jiang, *Mater. Lett.*, 2009, **63**, 78–80.

50 S. Zhao, Y. Wang, J. Dong, C.-T. He, H. Yin, P. An, K. Zhao, X. Zhang, C. Gao, L. Zhang, J. Lv, J. Wang, J. Zhang, A. M. Khattak, N. A. Khan, Z. Wei, J. Zhang, S. Liu, H. Zhao and Z. Tang, *Nat. Energy*, 2016, **1**, 16184.

51 S. Zhao, D. Chen, F. Wei, N. Chen, Z. Liang and Y. Luo, *Ultrason. Sonochem.*, 2017, **39**, 845–852.

52 F. Bonaccorso, A. Lombardo, T. Hasan, Z. Sun, L. Colombo and A. C. Ferrari, *Mater. Today*, 2012, **15**, 564–589.

53 J. Lopez-Cabrelles, S. Manas-Valero, I. J. Vitorica-Yrezabal, P. J. Bereciartua, J. A. Rodriguez-Velamazan, J. C. Waerenborgh, B. J. C. Vieira, D. Davidovikj, P. G. Steeneken, H. S. J. van der Zant, G. Minguez Espallargas and E. Coronado, *Nat. Chem.*, 2018, **10**, 1001–1007.

54 X. Wang, C. Chi, K. Zhang, Y. Qian, K. M. Gupta, Z. Kang, J. Jiang and D. Zhao, *Nat. Commun.*, 2017, **8**, 14460.

55 Y. Ding, Y. P. Chen, X. Zhang, L. Chen, Z. Dong, H. L. Jiang, H. Xu and H. C. Zhou, *J. Am. Chem. Soc.*, 2017, **139**, 9136–9139.

56 M. E. Logelin, E. Schreiber, B. Q. Mercado, M. J. Burke, C. M. Davis and A. K. Bartholomew, *Chem. Sci.*, 2024, **15**, 15198–15204.

57 A. I. Martín-Perales, T. Len, R. Esposito, I. Malpartida, R. Luque and A. Balu, *Inorg. Chem. Commun.*, 2024, **168**, 112813.

58 A. Gallego, C. Hermosa, O. Castillo, I. Berlanga, C. J. Gómez-García, E. Mateo-Martí, J. I. Martínez, F. Flores, C. Gómez-Navarro, J. Gómez-Herrero, S. Delgado and F. Zamora, *Adv. Mater.*, 2013, **25**, 2141–2146.

59 R. Dong, M. Pfeffermann, H. Liang, Z. Zheng, X. Zhu, J. Zhang and X. Feng, *Angew. Chem., Int. Ed.*, 2015, **54**, 12058–12063.

60 N. Lahiri, N. Lotfizadeh, R. Tsuchikawa, V. V. Deshpande and J. Louie, *J. Am. Chem. Soc.*, 2017, **139**, 19–22.

61 A. J. Clough, J. M. Skelton, C. A. Downes, A. A. de la Rosa, J. W. Yoo, A. Walsh, B. C. Melot and S. C. Marinescu, *J. Am. Chem. Soc.*, 2017, **139**, 10863–10867.

62 T. Kambe, R. Sakamoto, K. Hoshiko, K. Takada, M. Miyachi, J.-H. Ryu, S. Sasaki, J. Kim, K. Nakazato, M. Takata and H. Nishihara, *J. Am. Chem. Soc.*, 2013, **135**, 2462–2465.

63 M. Zhao, Y. Wang, Q. Ma, Y. Huang, X. Zhang, J. Ping, Z. Zhang, Q. Lu, Y. Yu, H. Xu, Y. Zhao and H. Zhang, *Adv. Mater.*, 2015, **27**, 7372–7378.

64 A. Pustovarenko, M. G. Goesten, S. Sachdeva, M. Shan, Z. Amghouz, Y. Belmabkhout, A. Dikhtiarenko, T. Rodenas, D. Keskin, I. K. Voets, B. M. Weckhuysen, M. Eddaoudi, L. C. P. M. de Smet, E. J. R. Sudhölter, F. Kapteijn, B. Seoane and J. Gascon, *Adv. Mater.*, 2018, **30**, 1707234.

65 F. Xue, P. Kumar, W. Xu, K. A. Mkhoyan and M. Tsapatsis, *Chem. Mater.*, 2018, **30**, 69–73.

66 X. Gao, R. Cui, M. Zhang and Z. Liu, *Mater. Lett.*, 2017, **197**, 217–220.

67 H. Fan, H. Yu, X. Wu, Y. Zhang, Z. Luo, H. Wang, Y. Guo, S. Madhavi and Q. Yan, *ACS Appl. Mater. Interfaces*, 2016, **8**, 25261–25267.

68 R. Dai, F. Peng, P. Ji, K. Lu, C. Wang, J. Sun and W. Lin, *Inorg. Chem.*, 2017, **56**, 8128–8134.

69 P. Wang, S. Song, M. He, C. Li, W. Wang, H. Li, X. Yuan, Z. Fang, K. P. Rinel, W. Song, J. Li, D. G. Vlachos and Z. Li, *Chem Catal.*, 2023, **3**, 100497.

70 R. R. Kimaka P, P. Wang, M. He, S. Meng, J. Yao, H. Li, C. Yang and Z. Li, *Sci. China:Chem.*, 2024, **67**, 2586–2598.

71 C. Yang, J. Yao, S. Meng, P. Wang, M. He, P. Li, P. Xiao, J. Xiao, Y. Liu and Z. Li, *J. Am. Chem. Soc.*, 2025, **147**, 9865–9878.

72 Z. Li, X. Zhang, Y. Kang, C. C. Yu, Y. Wen, M. Hu, D. Meng, W. Song and Y. Yang, *Advanced Science*, 2021, **8**, 2002631.

73 H. Sun, L. Chen, Y. Lian, W. Yang, L. Lin, Y. Chen, J. Xu, D. Wang, X. Yang, M. H. Rummerli, J. Guo, J. Zhong, Z. Deng, Y. Jiao, Y. Peng and S. Qiao, *Adv. Mater.*, 2020, **32**, e2006784.

74 X. Mu, H. Yuan, H. Jing, F. Xia, J. Wu, X. Gu, C. Chen, J. Bao, S. Liu and S. Mu, *Appl. Catal., B*, 2021, **296**, 120095.

75 D. Song, H. Guo, K. Huang, H. Zhang, J. Chen, L. Wang, C. Lian and Y. Wang, *Mater. Today*, 2022, **54**, 42–51.

76 P. He, P. Xie, Y. Dou, J. Zhou, A. Zhou, X. Wei and J. R. Li, *ACS Appl. Mater. Interfaces*, 2019, **11**, 41595–41601.

77 Z.-Y. Zhao, X. Sun, H. Gu, Z. Niu, P. Braunstein and J.-P. Lang, *ACS Appl. Mater. Interfaces*, 2022, **14**, 15133–15140.

78 K. Ge, S. Sun, Y. Zhao, K. Yang, S. Wang, Z. Zhang, J. Cao, Y. Yang, Y. Zhang, M. Pan and L. Zhu, *Angew. Chem., Int. Ed.*, 2021, **60**, 12097–12102.

79 W.-S. Liu, X. Hu, K. Zeng, C.-H. Ji, H. Feng, Y.-G. Zhou and Q.-Y. Cai, *J. Mater. Chem. A*, 2025, **13**, 3174–3184.

80 S. Zhang, Z. Huang, T. T. Isimjan, D. Cai and X. Yang, *Appl. Catal., B*, 2024, **343**, 123448.

81 W. Chen, C. Wang, S. Su, H. Wang and D. Cai, *Chem. Eng. J.*, 2021, **414**, 128784.

82 C. Ni, H. Zheng, W. Liu, L. Wu, R. Li, K. Zhou and W. Zhang, *Adv. Funct. Mater.*, 2023, **33**, 2301075.

83 Y. Liu, S. Deng, S. Fu, X. Wang, G. Liu and H. Yang, *J. Mater. Chem. A*, 2024, **12**, 8885–8892.

84 Z. Li, C. Yu, Y. Kang, X. Zhang, Y. Wen, Z. K. Wang, C. Ma, C. Wang, K. Wang, X. Qu, M. He, Y. W. Zhang and W. Song, *Natl. Sci. Rev.*, 2021, **8**, nwaa204.

85 D. Kobayashi, H. Kobayashi, D. Wu, S. Okazoe, K. Kusada, T. Yamamoto, T. Toriyama, S. Matsumura, S. Kawaguchi, Y. Kubota, S. M. Aspera, H. Nakanishi, S. Arai and H. Kitagawa, *J. Am. Chem. Soc.*, 2020, **142**, 17250–17254.

86 W. Zhang, W. Lai and R. Cao, *Chem. Rev.*, 2017, **117**, 3717–3797.

87 F.-L. Li, P. Wang, X. Huang, D. J. Young, H.-F. Wang, P. Braunstein and J.-P. Lang, *Angew. Chem., Int. Ed.*, 2019, **58**, 7051–7056.

88 Z. Xiao, Y. Wang, Y.-C. Huang, Z. Wei, C.-L. Dong, J. Ma, S. Shen, Y. Li and S. Wang, *Energy Environ. Sci.*, 2017, **10**, 2563–2569.

89 H. Huang, Y. Zhao, Y. Bai, F. Li, Y. Zhang and Y. Chen, *Advanced Science*, 2020, **7**, 2000012.

90 D. Zhu, J. Liu, Y. Zhao, Y. Zheng and S.-Z. Qiao, *Small*, 2019, **15**, 1805511.

91 C. Guo, Y. Jiao, Y. Zheng, J. Luo, K. Davey and S.-Z. Qiao, *Chem*, 2019, **5**, 2429–2441.

92 K. Rui, G. Zhao, M. Lao, P. Cui, X. Zheng, X. Zheng, J. Zhu, W. Huang, S. X. Dou and W. Sun, *Nano Lett.*, 2019, **19**, 8447–8453.

93 F. Yang, J. Xie, X. Liu, G. Wang and X. Lu, *Small*, 2021, **17**, 2007085.

94 W. Cheng, X. F. Lu, D. Luan and X. W. D. Lou, *Angew. Chem., Int. Ed.*, 2020, **59**, 18234–18239.

95 K. Huang, S. Guo, R. Wang, S. Lin, N. Hussain, H. Wei, B. Deng, Y. Long, M. Lei, H. Tang and H. Wu, *Chin. J. Catal.*, 2020, **41**, 1754–1760.

96 M. Wang, X. Dong, Z. Meng, Z. Hu, Y.-G. Lin, C.-K. Peng, H. Wang, C.-W. Pao, S. Ding, Y. Li, Q. Shao and X. Huang, *Angew. Chem., Int. Ed.*, 2021, **60**, 11190–11195.

97 Y. Liu, Q. Yan, F. Ge, X. Duan, T. Wu and H. Zheng, *J. Mater. Chem. A*, 2025, **13**, 4513–4520.

98 M. Wang, N. Zhang, Y. Feng, Z. Hu, Q. Shao and X. Huang, *Angew. Chem., Int. Ed.*, 2020, **59**, 14373–14377.

99 P. Wang, S. Meng, B. Zhang, M. He, P. Li, C. Yang, G. Li and Z. Li, *J. Am. Chem. Soc.*, 2023, **145**, 26133–26143.

100 Z.-Z. Niu, L.-P. Chi, R. Liu, Z. Chen and M.-R. Gao, *Energy Environ. Sci.*, 2021, **14**, 4169–4176.

101 X. Tan, C. Yu, Y. Ren, S. Cui, W. Li and J. Qiu, *Energy Environ. Sci.*, 2021, **14**, 765–780.

102 P. Wang, S. Meng, B. Zhang, M. He, P. Li, C. Yang, G. Li and Z. Li, *J. Am. Chem. Soc.*, 2023, **145**, 26133–26143.

103 M. Hu, J. Liu, S. Song, W. Wang, J. Yao, Y. Gong, C. Li, H. Li, Y. Li, X. Yuan, Z. Fang, H. Xu, W. Song and Z. Li, *ACS Catal.*, 2022, **12**, 3238–3248.

104 Y. Tian, C. Zhu, L. Yan, J. Zhao and Z. Su, *J. Mater. Chem. A*, 2019, **7**, 15341–15346.

105 M.-D. Zhang, D.-H. Si, J.-D. Yi, Q. Yin, Y.-B. Huang and R. Cao, *Sci. China:Chem.*, 2021, **64**, 1332–1339.

106 J.-D. Yi, D.-H. Si, R. Xie, Q. Yin, M.-D. Zhang, Q. Wu, G.-L. Chai, Y.-B. Huang and R. Cao, *Angew. Chem., Int. Ed.*, 2021, **60**, 17108–17114.

107 Q. Huang, X. Sha, R. Yang, H. Li and J. Peng, *ACS Appl. Mater. Interfaces*, 2024, **16**, 13882–13892.

108 Z. Zhao, X. Shen, X. Luo, M. Chen, M. Zhang, R. Yu, R. Jin and H. Zheng, *Adv. Energy Mater.*, 2024, **14**, 2400851.

109 Y. Zou, Y. Yan, Q. Xue, C. Zhang, T. Bao, X. Zhang, L. Yuan, S. Qiao, L. Song, J. Zou, C. Yu and C. Liu, *Angew. Chem., Int. Ed.*, 2024, **63**, e202409799.

110 H. Jiang, S. Bu, Q. Gao, J. Long, P. Wang, C.-S. Lee and W. Zhang, *Mater. Today Energy*, 2022, **27**, 101024.

111 L. Wang, Y. Zhu, Y. Wen, S. Li, C. Cui, F. Ni, Y. Liu, H. Lin, Y. Li, H. Peng and B. Zhang, *Angew. Chem., Int. Ed.*, 2021, **60**, 10577–10582.

112 D. Zhu, M. Qiao, J. Liu, T. Tao and C. Guo, *J. Mater. Chem. A*, 2020, **8**, 8143–8170.

113 A. Yuan, J. Du, Y. Zheng, H. Liu, H. Zhang, H. Li and L. Chen, *J. Colloid Interface Sci.*, 2025, **684**, 243–250.

114 H. Wang, H. Zou, Y. Liu, Z. Liu, W. Sun, K. A. Lin, T. Li and S. Luo, *Sci. Rep.*, 2021, **11**, 21414.